Journal of the Serbian Society for Computational Mechanics / Vol. 17 / No. 1, 2023 / pp 25-40
(10.24874/jsscm.2023.17.01.02)

NUMERICAL STUDY OF THE EFFECT OF TAPER ANGLES AND TAPER LENGTH ON THE REDUCTION OF AERODYNAMIC DRAG

Marouane Essahraoui[1], Rachid El Bouayadi[1], Mohammed El Ganaoui[2] and Aouatif Saad[1*]

[1] ASELAB, Advanced Systems Engineering Laboratory, National School of Applied Sciences, Ibn Tofail University, Kenitra, Morocco
e-mail: marouane.essahraoui@gmail.com, saad_aouatif@yahoo.fr, saad.aouatif@uit.ac.ma
[2] LERMAB/IUT Longwy, Institut Carnot, University of Lorraine, Nancy, France
**corresponding author*

Abstract

Aerodynamic drag is still one of the main challenges facing the automotive industry. The design engineers are trying to develop novel techniques that could help to control the flow and optimize the shape of a vehicle to make it able to increase the base pressure drag at the wake region. The pressure drag is one of the main contributors to the aerodynamic drag. In our investigation, we have dealt with a benchmark car model (Windsor geometry) and visualized its effect on the characteristic parameters of the flow. In order to maximize the reduction of aerodynamic drag of vehicles, a numerical study has been undertaken based upon the CFD analysis with an active flow control technique including tapering of the rear lower and upper body along the length and height of the Windsor geometry. Taper angles from 12° to 20° in 4° steps have been implemented on the upper and lower part of the body while a taper length has been implemented along with the height of the body sides for the two cases. In comparison to other studies, we have come to sufficient results that gave us a significant reduction of aerodynamic drag for all the cases that we have tested. Thus, our study showed that the aerodynamic drag reductions are maximized, which indicates the efficiency of the technique we have applied.

Keywords: Turbulent, base pressure drag, CFD, active flow control, lift, tapering, k-epsilon.

1. Introduction

Our planet is faced with many threats, and our role is to tackle them. Researchers are working in advance to optimize the energy sources in an attempt to minimize gas emissions and enhance CO_2 regulations. The automotive industry contributes 9% in the annual global greenhouse emissions; thus, improving and enhancing the geometry of vehicles is required for a better reduction of pressure drag, which contributes in more than 80% of total aerodynamic drag. The reduction in aerodynamic drag leads to better CO_2 regulations and a reduction in gas emissions. Because of that, the design engineers are working under pressure to optimize the flow control methods in order to enhance vehicles' roads.

Passive or active methods are both applied in an attempt to increase the base pressure drag by affecting the recirculation wake region due to boundary layer separation. Among the active

flow methods mentioned is the experimental study of Bideaux et al. (2011) who applied the air jets method to control the flow on the rear part of the Ahmed body geometry in a wind tunnel, Heinemann, Springer, Lienhart, Kniesburges and Becker (2012) applied the steady blowing method in an attempt to visualize the variation of drag and lift through a continuous slot at the rear window; and Littlewood and Passmore (2012) applied the same method of steady blowing but on a ¼ square back vehicle with a variety of angles on the roof of the trailing edge of the geometry. Aerodynamics research on a basic car model with a variety of alternative car models was carried out by Prajwal, Unune and Aherwar (2015) in a wind tunnel operating at a low speed. An experimental study by Jahanmiri & Abbaspour (2011) has shown the effect of suction and base bleeding on the aerodynamic drag reduction of Ahmed's body with a 35° rear slant angle. The application of active flow control methods helps to achieve a significant reduction in aerodynamic drag. Otherwise, there are other types of research and active methods we have not mentioned that have shown their capability to reduce aerodynamic drag, such as strip pulse jets, and synthetic jets. While the passive control flow consists of modifying the shape of vehicles or attaching add-on devices to decrease the aerodynamic drag, we will mention vortex generators, and according to van de Wijdeven and Katz (2014) who have studied the distribution of pressure upon the surface and the trailing vortex signature behind the VG's of a generic model in a low-speed wind tunnel, the main object of implementing the VG's is to manipulate the boundary layer. Another control flow method has been carried out by Hu and Wong (2011) who studied the effect of spoilers on aerodynamic drag with and without a rear-spoiler by using a CFD simulation. Kodali and Bezavada (2012) also applied the same method to a 3D vehicle with a rear spoiler, and the results showed a significant reduction in aerodynamic drag.

The research review (Sudin, Abdullah, Shamsuddin, Ramli, & Tahir, 2014) states that both passive and active flow control approaches can minimize aerodynamic drag, although some researchers have favored the active methods due to their adaptability in a variety of applications. Mariaprakasam et al. (2023) suggest that we can combine the two techniques in an effort to reduce drag effectively while taking a number of restrictions into consideration.

Taper angle and taper length have been analysed experimentally in the study of Howell, Passmore and Tuplin (2013). So, in our study, we have tried to apply the taper angle and taper length with the 3-taper length technique distributed along the height of the Windsor body and various taper angles in the upper and lower bodies upon the Windsor body. In the first case, we tapered the upper part with a taper angle from 12° to 20° while the lower part was un-tapered, and in the second case, we tapered the lower part with a taper angle from 12° to 20° with a fixed taper angle of 4° on the upper part. According to the literature, we have tried to modify the Windsor geometry by applying a new method to the lower and upper parts for the design and numerical calculations for parametric flow. In all cases that we applied, we achieved a sufficient result for aerodynamic drag reduction and lift.

2. Physical and numerical methods

2.1 Mathematical formulations

$$\frac{\partial u_i}{\partial x_i} = 0 \tag{1}$$

$$\frac{\partial \overline{u_i}}{\partial t} + \overline{u_j}\frac{\partial \overline{u_i}}{\partial x_j} = -\frac{1}{\rho}\frac{\partial \bar{p}}{\partial x_i} + \nu\frac{\partial^2 \overline{u_i}}{\partial x_j^2} - \frac{\partial \overline{u_i' u_j'}}{\partial x_j} \tag{2}$$

$$\frac{\partial \rho k}{\partial t} + \frac{\partial \rho k u_i}{\partial x_i} = \frac{\partial}{\partial x_j}\left[\left(\mu + \frac{\mu_T}{\sigma_k}\right)\frac{\partial k}{\partial x_j}\right] + G_k - \rho\varepsilon \tag{3}$$

$$\frac{\partial \rho \varepsilon}{\partial t} + \frac{\partial \rho \varepsilon u_i}{\partial x_i} = \frac{\partial}{\partial x_j}\left[\left(\mu + \frac{\mu_T}{\sigma_\varepsilon}\right)\frac{\partial \varepsilon}{\partial x_j}\right] + C_{1\varepsilon}\frac{\varepsilon}{k}(G_k) - C_{2\varepsilon}\rho\frac{\varepsilon^2}{k} \quad (4)$$

Equation (1) relates to the continuity equation for incompressible flow, wherein the density of the system remains constant. This implies that the mass density, represented by the symbol ρ remains constant across both time and space (Ronald, 2013). The continuity equation for incompressible fluids is a valuable tool in the field of fluid mechanics and is frequently utilized to investigate diverse flow phenomena, including but not limited to pipe flows, channel flows, and aerodynamics. This phenomenon offers valuable insights into the behavior of fluids that cannot be compressed, aiding in the comprehension of fluid conservation and the manner in which velocities are distributed within a flow field. According to (Ronald, 2013), the symbol $\frac{\partial u_i}{\partial x_i} = 0$ denotes the divergence of the velocity vector.

Equation (2) denotes the Reynolds averaging-Navier-Stokes (RANS) equation. The Reynolds-averaged Navier-Stokes (RANS) equations are a mathematical formulation obtained by utilizing the Reynolds averaging method on the Navier-Stokes equations. The Reynolds averaging methodology is employed to incorporate the turbulent fluctuations present in the flow field. The Reynolds-averaged Navier-Stokes (RANS) equations involve the decomposition of flow variables, including velocity and pressure, into their respective time-averaged mean components and fluctuating components, as described by Pattijn (1999) The process of time-averaging is symbolized by an overbar (e.g., $\overline{u_{i,j}}, \bar{p}$) which signifies the mean values of the corresponding variables. The prime symbol (e.g., u_i', u_j', p') is utilized to denote the fluctuating components. The symbols $\partial \overline{u_i' u_j'}$ denote the partial differential of the Reynolds stress tensor, which is responsible for capturing the turbulent fluctuations in the fluid flow (Pattijn, 1999).

Equations (3) and (4) denote the transport equations governing the turbulent kinetic energy (TKE) and turbulent dissipation rate (epsilon), correspondingly. The states of turbulent kinetic energy serve as a metric for quantifying the amount of energy present in flow fluctuations. Meanwhile, the turbulent dissipation rate serves as a metric for measuring the rates at which turbulent kinetic energy is dissipated. These metrics are represented by various symbols, including μ_T for turbulent viscosity, $\rho k u_i$ for advective flux of TKE, and $\left(\mu + \frac{\mu_T}{\sigma_k}\right)\frac{\partial k}{\partial x_j}$ for diffusive flux of TKE due to turbulent viscosity. Additionally, ε represents the TKE dissipation rate, and G_k represents the production of TKE, as noted by Pattijn (1999). The coefficients present in equation (4) are based on empirical data. The standard $k - \varepsilon$ model was selected for our study, resulting in the following values for the empirical coefficients:
$\mathrm{C}_{1\varepsilon} = 1.44, \mathrm{C}_{2\varepsilon} = 1.92, \sigma_\mathrm{k} = 1.0, \sigma_\varepsilon = 1.3, \mathrm{C}_\mu = 0.09$

2.2 Numerical methods

The impact of airflow around a benchmark model (Windsor geometry) has been investigated through numerical simulations. The governing equations, which were steady, incompressible, and three-dimensional, were solved using the Fluent solver. The realizable k-epsilon turbulence model was utilized by the ANSYS Fluent solver. ANSYS Fluent was selected due to its user-friendly interface in comparison to other available software options. Fluent has been recognized as one of the top finite volume solvers for the simulation of steady incompressible airflow in the context of solving pre-discretized models. The present study concerns the turbulence phenomenon that arises in the vicinity of the rear portion of the geometry. Various numerical simulations, including DNS, LES, and RANS, have been employed to address this issue. The RANS (Reynolds Averaged Navier-Stokes) equation was selected for our study due to its relatively low computational cost and satisfactory accuracy, compared to the other available techniques. The Reynolds-Averaged Navier-Stokes (RANS) equations in their unsteady form are

capable of modeling time-dependent mean flows. However, for a variety of turbulent flows, including those around ground vehicles, it is often more practical and accurate to utilize the steady RANS equations. This approach allows for an economical and precise representation of these flows (Makowski and Kim, 2000). The utilization of the $k-\varepsilon$ turbulence model was implemented through the application of a second-order scheme. The simulated instances were subjected to a uniform inlet velocity of 45 $^{m}/_{s}$. The velocity in question pertains to the movement of an incompressible fluid with a Mach number below 0.3, flowing in a left-to-right direction, as depicted in Figure 1(a). In scenarios where flow velocities are relatively low, the pressure-based approach is deemed the most suitable method for simulating the flow of an incompressible fluid. To reduce numerical inaccuracies, the convergence threshold for pressure and velocity was established at 1×10^{-6} and 1×10^{-8}, correspondingly.

2.3 Geometrics and meshing

The virtual wind tunnel and the target body were subjected to an unstructured mesh application using ANSYS Mesh. Fig. 1 illustrates the fluid domain, wherein a fine mesh has been generated around the target body. Additionally, two inner boxes have been created in the proximity of the target body for all cases. The purpose of this approach is to obtain a finer mesh size in the regions surrounding the surface body and the wake region immediately behind it. This is aimed at accurately capturing the recirculating flow behavior that is responsible for the base pressure drag. In light of the geometric symmetry, we opted to utilize only half of the Windsor geometry in our model as a means of reducing the overall number of elements count N_b, which amounted to roughly $N_b = 2 \times 10^6$ elements throughout our investigation. The present investigation employs a Windsor geometry, as explained in the paper by Passmore, Gaylard and Pavia (2016) and implements an active flow control method on the geometry's rear and side edges. The utilization of taper length and taper angle on the rear part of the geometry was demonstrated in the studies conducted by Howell, Passmore and Tuplin (2013). Similarly, Varney, Passmore, Swakeen and Gaylard (2020) applied span tapering to the lower and upper rear parts of the geometry. Based on the findings of these studies, novel approaches have been explored in an endeavor to attain a noteworthy outcome in the reduction of aerodynamic drag. Consequently, a taper length has been implemented on the side edge, which is distributed throughout the height of the geometry. Additionally, a taper angle has been introduced in the upper and lower regions of the geometry, with three distinct taper angles ranging from 12 to 20 degrees in increments of 4 degrees. The virtual tunnel's dimensions are specified as follows: The dimensions of the geometry were reported as $18m \times 6m \times 3m$ (length, height, depth). As per the methodology proposed by Axelsson, Ramnefors and Gustafsson (1998), the geometry was positioned at a distance more than 5 meters from the inlet section. Alternatively, by exploiting the symmetry of Windsor geometry, the simulation was developed using only a portion of the geometry, as noted by Jorge Esteban Chavez, Luis Emilio Vera and Amir Antonio Martins (2020) study. The fluid domain, the various case geometries, and the computational meshes are depicted visually below. Fig. 1 displays the dimensions along the x, y, and z axes, as well as the mesh generation. The fluid domain, the position of the taper technique, and the upper and lower taper angles are depicted in the illustration. Figures 2 to 7 illustrate the inclination angles (12, 16 and 20 degrees) of the upper and lower taper in order to distinguish between each scenario. The back side of the geometry was subjected to both upper and lower taper techniques, with the taper length being applied to the rear side.

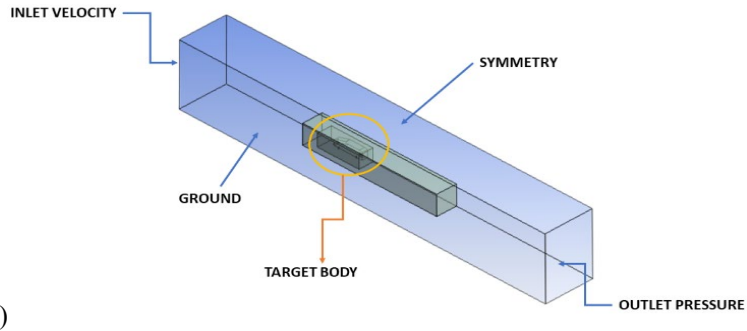

(a)

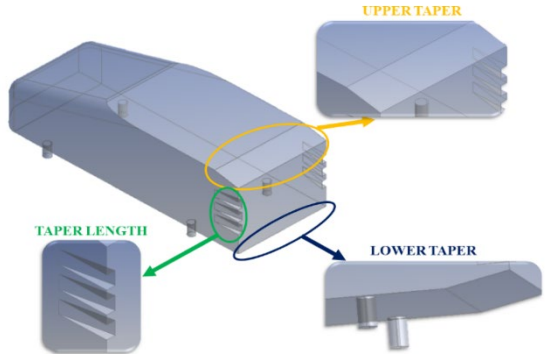

(b)

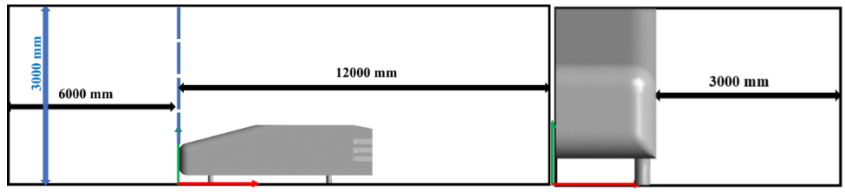

(c)

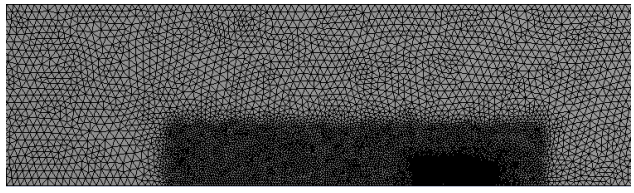

(d)

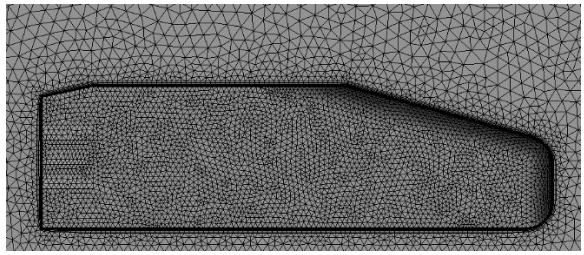

(e)

Fig. 1. (a) Fluid domain, (b) Taper length, Upper and Lower taper locations, (c) Dimensions, (d) Computational meshes in the symmetric plane, (e) Mesh zoom-in view around the target body.

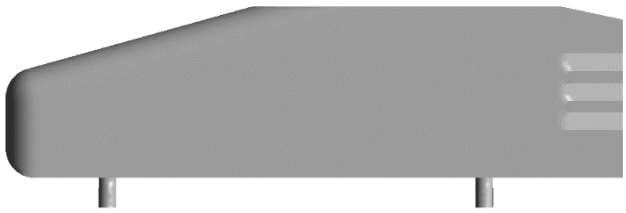

Fig. 2. Upper taper angle 12 degree.

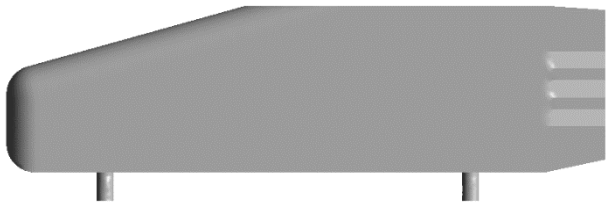

Fig. 3. Lower taper angle 12 degree.

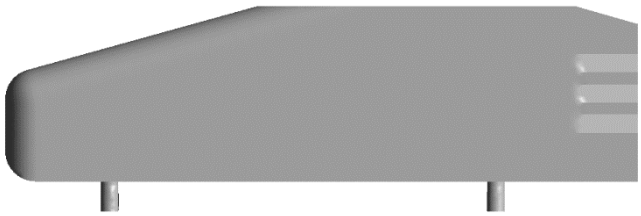

Fig. 4. Upper taper angle 16 degree.

Fig. 5. Lower taper angle 16 degree.

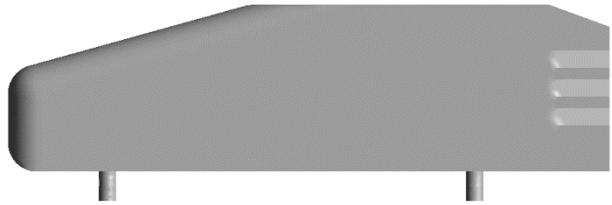

Fig. 6. Upper taper angle 20 degree.

Fig. 7. Lower taper angle 20 degree.

The boundary conditions and discretization scheme that have been used in this study will be cited in a table as follows according to Sebben (2004):

Fluid	Air
Solid	Aluminum
Velocity inlet	45 $^{m}/_{s}$
Density	1.225 $^{Kg}/_{m^3}$
Viscosity	1.7894E-04
Pressure outlet	Ambient (Gauge 0)
Windsor body	No slip condition

Table 1. Boundary conditions.

Pressure	Second Order
Momentum	Second Order Upwind
Turbulent Kinetic Energy	Second Order Upwind
Turbulent Dissipation Rate	Second Order Upwind

Table 2. Discretization scheme.

2.4 Characteristic parameter

The equations below represent a very important parameter which describes how the flow behavior changes and the force acting on the object while it is in contact with the fluid.

$$C_d = \frac{2F_d}{\rho V_\infty^2 A} \tag{5}$$

$$C_l = \frac{2F_l}{\rho V_\infty^2 A} \tag{6}$$

The equations (5) and (6) represent the coefficients of drag and lift respectively which are the primary characteristic factors that must be understood in order to have a better understanding of how fluid moves around a vehicle. Drag coefficient is a measure of the resistance encountered by an object moving through a fluid. It quantifies the ratio of drag force experienced by the object to the dynamic pressure of the fluid flow. The drag coefficient depends on the shape of the object, its orientation, and the properties of the fluid. It is given by the formula in equation (5) (Yasuki, 2018). Lift coefficient is a measure of the lift force generated by an object moving through a fluid, perpendicular to the direction of motion. It quantifies the ratio of the lift force to the dynamic pressure of the fluid flow. The lift coefficient depends on the shape of the object, its orientation, and the properties of the fluid. It is given by the formula in equation (6) (Yasuki, 2018). Where F_d *and* F_l are the forces acting opposite and perpendicular to the direction of motion respectively, A is the reference area of the object perpendicular to the flow direction, ρ mass density of the fluid, and V_∞^2 is the relative velocity between the object and the fluid.

$$C_f = \frac{\tau_w}{\frac{1}{2}\rho V_\infty^2} \tag{7}$$

Moreover, the equation (7) represents the skin friction coefficient which is a dimensionless quantity that defines the aerodynamic resistance owing to the contact of moving fluid on the surface of the vehicles. It measures the ratio of the skin friction force to the dynamic pressure of the fluid flow. The skin friction coefficient is commonly used in aerodynamics and fluid dynamics to assess the drag forces acting on an object. It depends on several factors, including the surface roughness of the body, the viscosity of the fluid, and the flow conditions. It is typically determined experimentally or calculated through theoretical or computational methods. The resistance is caused by the skin of the vehicle pressing against the fluid (Elbing, 2009) where τ_w is the wall shear stress, which represents the tangential force per unit area acting on the surface of the body.

$$C_P = \frac{P - P_\infty}{\frac{1}{2}\rho V_\infty^2} \tag{8}$$

The pressure coefficient is a term that does not have any dimensions and is used to define the relative pressure in the flow field. It is defined in the equation (8). It provides information about the variation in pressure compared to a reference pressure, typically the ambient or freestream pressure. The pressure coefficient is useful for analyzing aerodynamic forces, lift and drag distributions, and flow patterns around objects. In aerodynamics, the pressure coefficient is often represented graphically using pressure contour plots or pressure coefficient distributions over the surface of an airfoil or other objects. These plots provide valuable information about the lift and drag characteristics, separation points, and flow behavior around the object (Costola, Blocken, & Hensen, 2009) where P is the local pressure at a specific point on the surface, and P_∞ is the reference pressure (ambient or freestream pressure).

$$S_t = \frac{fL}{V_\infty} \tag{9}$$

For the purpose of studying vortex shedding, the Strouhal number provides a description of the oscillating flow process which is defined in the equation (9). It is a dimensionless quantity used in fluid dynamics to describe the behavior of periodic or oscillatory flows (Essahraoui, El Bouayadi, & Saad, 2022). It relates the frequency of vortex shedding or periodic motion to the flow velocity and characteristic length of the object. The Strouhal number is also used to estimate the optimal frequency for energy harvesting from fluid flows. By understanding the Strouhal number associated with a particular flow regime, engineers can design devices or systems that

efficiently capture and convert flow-induced oscillations into useful energy (Williamson, 1996). Where f is the frequency of the vortex shedding or periodic motion, and L is a characteristic length of the object or the distance traveled per cycle.

3. Results and discussion

Cooper (2003) and Fred, Charles and Mathieu (2005) have conducted studies on the application of boat-tailing with a taper technique and the implementation of flaps along the rear side and roof with varying angles ranging from 10° to 20° in steps of 3 degrees, respectively. Both studies have identified an optimal angle for trucks. Cooper (2003) identified an optimal angle of approximately16°, while Fred, Charles and Mathieu (2005) found an optimal angle range of 20°-22°. The aforementioned studies have provided insight that prompted us to concentrate on particular angles in order to comprehend the impact of taper length and angles on the mitigation of aerodynamic drag. Taper angles ranging from 12° to 20° in increments of 4 degrees were implemented on both the upper and lower rear portions of the Windsor model. Additionally, the taper length on the rear side was distributed proportionally with the height of the Windsor model. The presented Figures (2-7) depict the entirety of the cases that have been submitted for consideration. The upper portion was tapered utilizing taper angles ranging from 12° to 20°, while the lower portion remained un-tapered in the initial scenario. In the second scenario, the lower portion has been tapered utilizing taper angles ranging from 12° to 20°, while the upper portion features a taper angle of 4°.

3.1 Variation of drag and lift coefficient upper and lower body taper

The data obtained for drag and lift for all cases are depicted in Figs. 8 and 9. The aerodynamic drag coefficient was found to be most optimal at a taper angle of 12° for the rear upper body taper, resulting in a value of $C_d = 0.256$. In contrast to square back data where $C_d = 0.297$, a reduction in drag of approximately 12% was observed. Furthermore, an increase in taper angles resulted in a continuous increase in the value of the aerodynamic drag coefficient. However, an unexpected decrease in drag occurred in the case of lower body taper for a taper angle of 16°, resulting in a decrease in the value of the aerodynamic drag coefficient. The obtained data illustrate the impact of taper angles on the fluctuation of the drag coefficient, consequently resulting in a variation of pressure in the wake region.

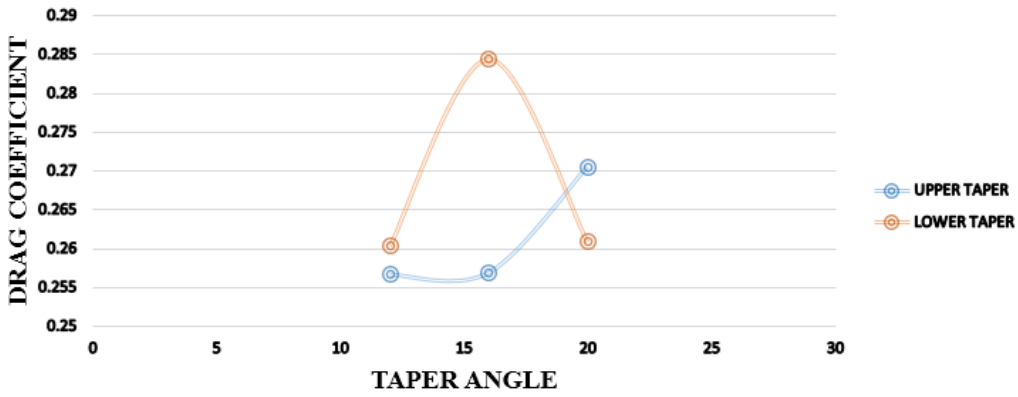

Fig. 8. Variation of drag coefficients for upper and lower body taper.

The lift coefficient is influenced by the taper of both the upper and lower body. The data reveal that lift coefficients can exhibit both positive and negative values. Fig. 9 depicts two cases of tapering: the upper body taper case is represented by positive values, whereas the lower body taper case is represented by negative values. The study on upper and lower body taper revealed a positive correlation between lift and taper angles. Additionally, Albert and Benjamin (2015) observed that the occurrence of negative lift in the context of lower body taper signifies the manifestation of a downforce in the Windsor model.

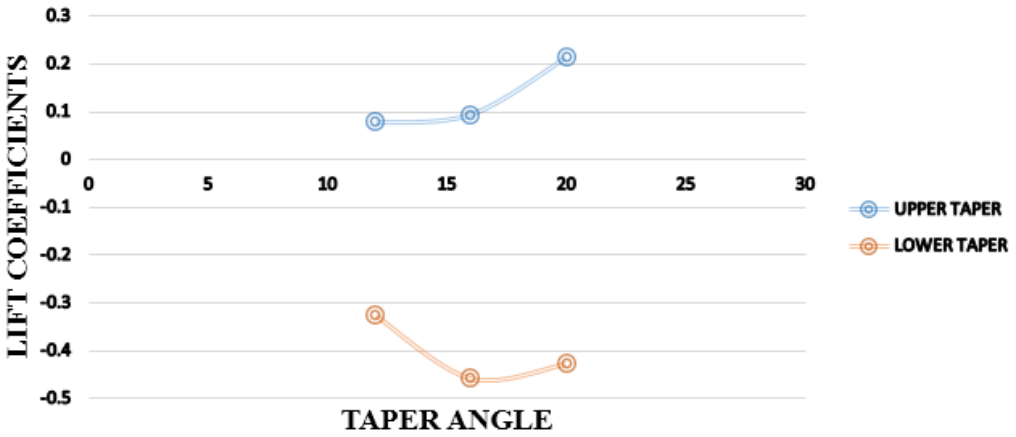

Fig. 9. Variation of lift coefficients for upper and lower body taper.

3.2. Pressure coefficient along the centerline of upper and lower body taper

The pressure coefficients (C_p) distribution along the centerline of the upper body taper and lower body taper are illustrated in Figs. 10 and 11. The pressure coefficients distribution on the top and bottom surfaces of the Windsor model is depicted by the curves, according to the findings (Young, Soo, Hee and Kunio, 2016) documented in the literature. Positive pressure values are observed at the leading edge of the Windsor model upon air impact, while negative pressure values are detected at the trailing edge. These pressure variations are attributed to alterations in pressure at the rear section of the Windsor model. The curves demonstrate that C_p values reach zero when $\frac{X}{L} = 1$, signifying a low-pressure area. This observation suggests the presence of a high separation flow at the rear portion of the object. Young, Soo, Hee and Kunio (2016) suggest that pressure variations at the rear part were primarily caused by blockage effects in the small computational domain. The pressure coefficients depicted in Figs. 10 and 11 for each taper angle value can be denoted as (C_p 12; C_p 16; C_p 20).

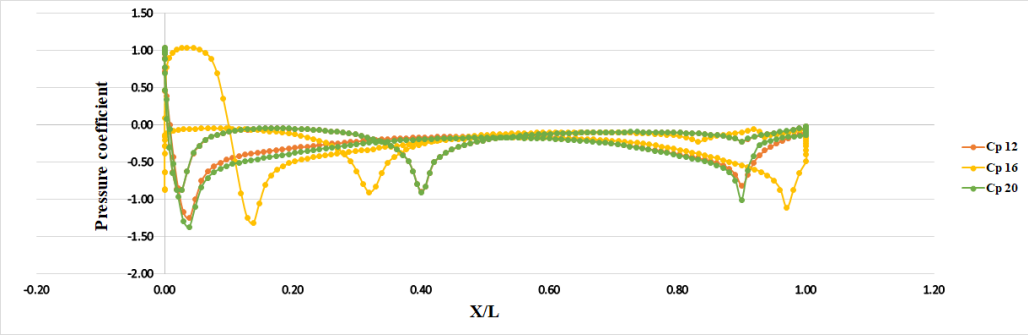

Fig. 10. Distribution of pressure coefficient along the centerline of lower body taper.

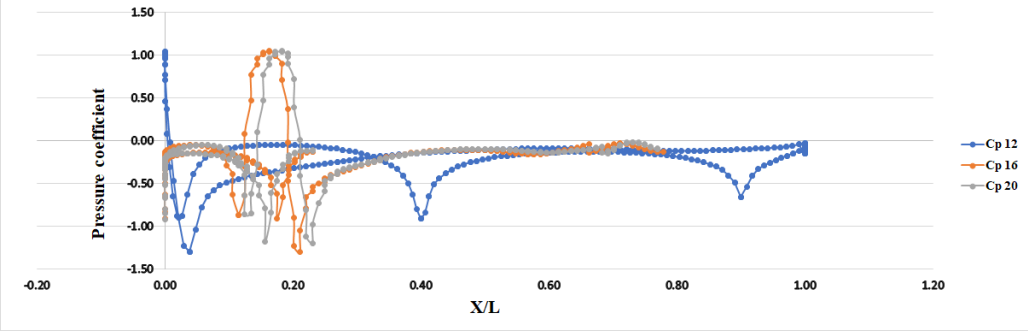

Fig. 11. Distribution of pressure coefficient along the centerline of upper body taper.

3.3 Velocity distribution along the upper and lower body taper

The figures below illustrate the magnitude of the velocity at the lateral position, represented by $y = 0$. The statement holds true across all model scenarios. Several experiments have indicated that the body's influence on the flow field results in the development of a high-velocity zone above the vehicle's top. Additionally, low-speed regions with separated flow are observed between these regions. Upon examining the numerical values in conjunction with the drag and lift metrics, it becomes evident that changes in taper angles exert an influence on the velocity within the wake area across all instances. Moreover, upon examining the lowercase, it is evident that the Windsor model's wake produces greater drag compared to the upper body case's wake. The relationship between base pressure, drag values, and velocity is such that an increase in the former two parameters will result in an increase in the latter. This phenomenon is consistent with Bernoulli's equation, which suggests that areas with high velocities correspond to low pressure. In instances where high velocities still exist in a particular region, separation may occur. Upon conducting a comparative analysis between the upper and lower body cases, it is evident that the lower case exhibits a greater drag coefficient, a more noticeable wake, and a larger low-speed region in the vehicle's wake. All of these characteristics are readily apparent when conducting this comparison. Enhancing the size and shape of the wakes can potentially lead to a reduction in the total drag magnitude. The primary aim of this study is to examine the impact of taper length and angle on the base wake.

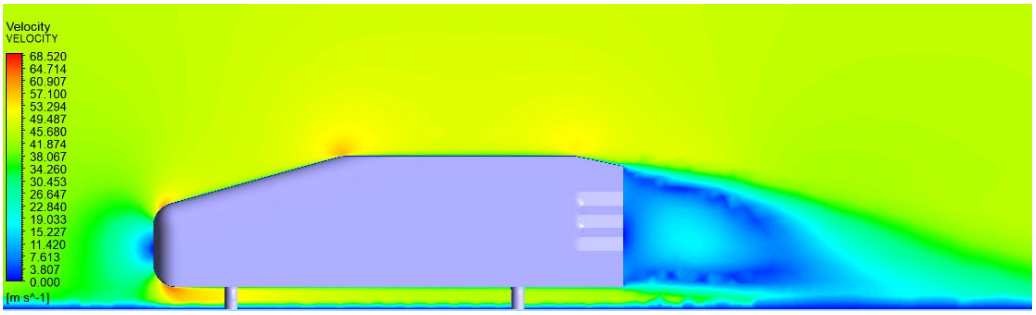

Fig. 12. Velocity distribution of the upper body taper angle 12 degree.

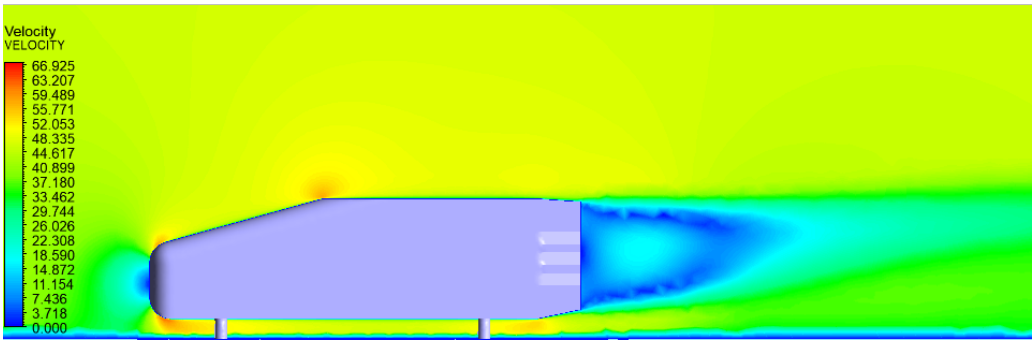

Fig. 13. Velocity distribution of the lower body taper angle 12 degree.

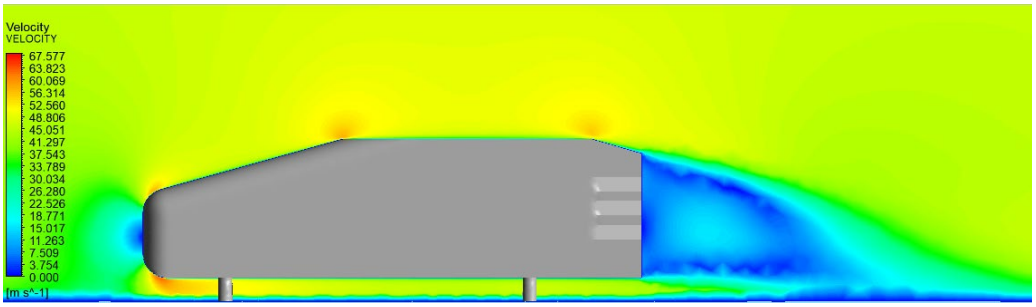

Fig. 14. Velocity distribution of the upper body taper angle 16 degree.

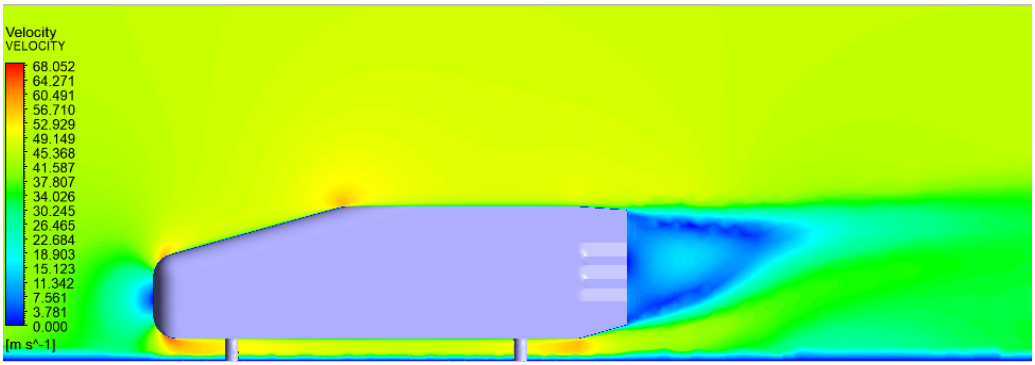

Fig. 15. Velocity distribution of the lower body taper angle 16 degree.

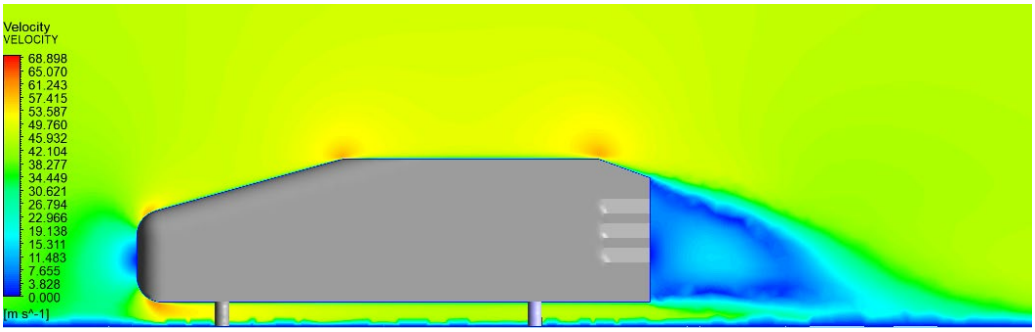

Fig. 16. Velocity distribution of the upper body taper angle 20 degree.

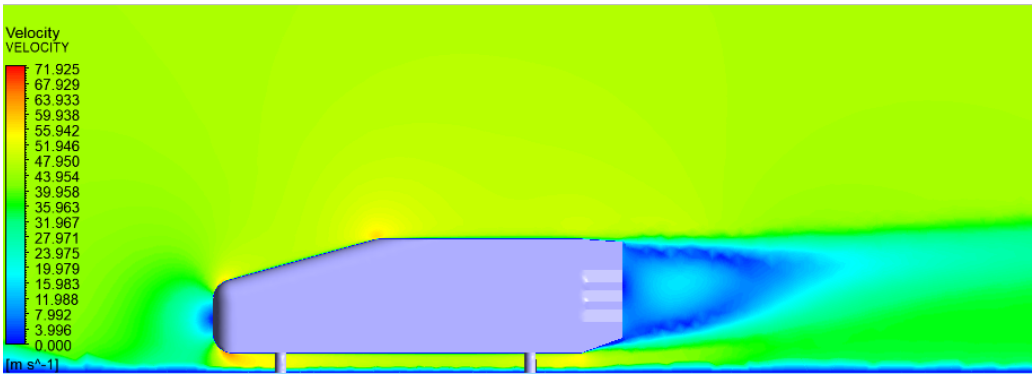

Fig. 17. Velocity distribution of the lower body taper angle 20 degree.

4. Conclusions

The present investigation has implemented diverse taper angles while maintaining a uniform taper length on the Windsor body aspect. Taper angles have been implemented on the upper and lower regions of the Windsor body, while taper length has been distributed proportionally to the body's height. This measure has been taken to reduce the amount of aerodynamic drag.

A comparative analysis was conducted between the drag and lift measurements and the square-back model. By implementing a taper angle of 12 degrees at the upper body, we were able to attain the optimal value, indicating a reduction of 12% in the generated aerodynamic drag. Likewise, an optimal lift coefficient value was determined for the same taper angle scenario through comparable means. The drag and lift data exhibited an anomalous result in the scenario where the lower body was tapered, featuring a taper angle of 16 degrees. The present study reveals that the aerodynamic drag coefficient holds an approximate equivalence to the square back drag coefficient. The lift coefficient values obtained for the lower taper cases were observed to be negative, indicating that the Windsor geometry produces a downward force. This deduction was drawn based on the data analysis.

The pressure coefficient graphs in the context of the upper body taper demonstrated the pressure distribution across the body's surface. The reattachment of fluid on the surface of Windsor occurs at taper angles that fall within the range of 16 to 20 degrees. The numerical values underwent a significant reduction to attain negative pressure coefficients, which would lead to fluid separation and a subsequent rise in the drag coefficient.

In cases where the lower body tapers, the Windsor body may experience instability due to a reduction in velocity along the x-direction. This decrease in velocity can lead to a significant drop in pressure behind the body, ultimately resulting in a negative lift coefficient. This factor could potentially contribute to the production of downforce and result in decreased stability of the Windsor body. In addition, the tapering of the upper body indicates that our findings are comparable to the information regarding drag coefficients. The study revealed that an increase in the angle of the taper led to a reduction in the pressure region, thereby causing a corresponding increase in drag.

One of the objectives of our research was to create a technique that would gradually decrease the dimensions of a Windsor body towards its rear end, with the aim of achieving the minimum attainable amount of aerodynamic resistance.

Acknowledgements: We express our gratitude to the University of Lorraine, Nancy, France for their computational support.

References

Albert, B. and Benjamin, M. (2015). Analysis of lift and drag coefficients of a GT2 racing car at various speeds with movable wheels and ground. World Journal of Engineering, 12(3), 261-270.

Axelsson, N., Ramnefors, M. and Gustafsson, R. (1998). Accuracy in computational aerodynamics Part 1: Stagnation pressure. SAE transactions, 223-233.

Bideaux, E., Bobillier, P., Fournier, E., Gilliéron, P., Hajem, M., Champagne, J. Y. and and Koutra, A. (2011). Drag reduction by pulsed jets on strongly unstructured wake: towards the square back control. International Journal of Aerodynamics, Vol.1(3), 282-298.

Cooper, K. R. (2003). Truck Aerodynamics Reborn-Lessons from the Past.

Costola, D., Blocken, B. and Hensen, J. M. (2009). Overview of pressure coefficient data in building energy simulation and airflow network programs. Building and environment, 44(10), 2027-2036.

Elbing, B. R. (2009). Skin-friction drag reduction within turbulent flows. University of Michigan. Retrieved from https://hdl.handle.net/2027.42/62411

Essahraoui, M., El Bouayadi, R. and Saad, A. (2022). The effect of rotation rates, cylinder diameter and lateral boundaries on strouhal number in unsteady regimes at different reynolds numbers. Journal of the Serbian Society for Computational Mechanics, 16(2), 56-66.

Fred, B., Charles, R. and Mathieu, B. (2005). Fuel Savings by Means of Flaps Attached to the Base of a Trailer: Field Test Results.

Heinemann, T., Springer, M., Lienhart, H., Kniesburges, S. and Becker, S. (2012). Active flow control on a 1: 4 car model. In 16th Int Symp on Applications of Laser Techniques to Fluid Mechanics. Lisbon, Portugal.

Howell, J., Passmore, M. and Tuplin, S. (2013). Aerodynamic Drag Reduction on a Simple Car-Like Shape with Rear Upper Body Taper. SAE Int. J. Passeng. Cars-Mech. Syst, Vol.6(1), 52-60.

Hu, X. X. and and Wong, T. T. (2011). A numerical study on rear-spoiler of passenger vehicle. World Academy of Science, Engineering and technology, Vol.57, 636-641.

Jahanmiri, M. and Abbaspour, M. (2011). Experimental investigation of drag reduction on ahmed model using a combination of active flow control methods. International Journal of Engineering-Transactions A: Basics, Vol.24(4), 403-410.

Jorge Esteban Chavez, G., Luis Emilio Vera, D., and Amir Antonio Martins, O. (2020). The Ahmed body's external aerodynamics at 25° slant angle rear surface: a numerical analysis using cfd. 18th Brazilian Congress of Thermal Sciences and Engineering (pp. 1-11). encit 2020.

Kodali, S. P. and Bezavada, S. (2012). Numerical simulation of air flow over a passenger car and the Influence of rear spoiler using CFD. International Journal of Advanced Transport Phenomena, Vol.01(1), 6-31.

Littlewood, R. P. and Passmore, M. A. (2012). Aerodynamic drag reduction of a simplified squareback vehicle using steady blowing. Experiments in fluids, Vol.53(2), 519-529.

Makowski, F. T. and Kim, S. E. (2000). Advances in external-aero simulation of ground vehicles using the steady RANS equations. SAE Technical Paper 2000-01-0484.

Mariaprakasam, R. R., Mat, S., Samin, P. M., Othman, N., Ab Wahid, M. and Said, M. (2023). Review on Flow Controls for Vehicles Aerodynamic Drag Reduction. Journal of Advanced Research in Fluid Mechanics and Thermal Sciences, 101(1), 11-36.

Passmore, M., Gaylard, A. and Pavia, G. (2016). Influence of Short Rear End Tapers on the Unsteady Base. Experiments in Fluids, 57(11), 1-17.

Pattijn, S. (1999). Non-linear, low-Reynolds, two-equation turbulence models. GENT. Retrieved from https://www.fem.unicamp.br/~phoenics/SITE_PHOENICS/Apostilas/PHD_Tesis_S.%20Pattijn/Chapters/chapter02.pdf

Prajwal, B., Unune, D. and Aherwar, A. (2015). Modelling, simulation and validation of results with different car models using wind tunnel and Star-CCM+. Journal of Serbian Society for Computational Mechanics, 9(1), 46--56.

Ronald, L. P. (2013). Incompressible flow. John Wiley & Sons.

Sebben, S. (2004). Numerical simulations of a car underbody: effect of front-wheel deflectors. SAE Technical Paper.

Sudin, M. N., Abdullah, M. A., Shamsuddin, S. A., Ramli, F. R. and Tahir, M. M. (2014). Review of research on vehicles aerodynamic drag reduction methods. International Journal of Mechanical and Mechatronics Engineering, 14(02), 37-47.

van de Wijdeven, T. and Katz, J. (2014). Automotive application of VGs in ground effect. Journal of Fluids Engineering, Vol.136(2).

Varney, M., Passmore, M., Swakeen, R. and Gaylard, A. (2020). Parametric study of reduced span side tapering on a simplified model with wheels.

Williamson, C. H. (1996). Vortex dynamics in the cylinder wake. Annual review of fluid mechanics, 28(1), 477-539.

Yasuki, N. (2018). Introduction to Fluid Mechanics (Second Edition). Butterworth-Heinemann. Retrieved from https://www.sciencedirect.com/science/article/pii/B9780081024379000097

Young, T. L., Soo, L. B., Hee, C. L. andKunio, M. (2016). Pressure distribution on rectangular buildings with changes in aspect ratio and wind direction. Wind and Structures, 23(5), 465-483.